

PAPER

Production of exotic neutron-deficient isotopes ^{*} near $N, Z = 50$ in multinucleon transfer reactions ^{*}

To cite this article: Xin-Xin Xu *et al* 2019 *Chinese Phys. C* **43** 064105

View the [article online](#) for updates and enhancements.

You may also like

- [Mass predictions of the relativistic continuum Hartree-Bogoliubov model with radial basis function approach](#)

Min Shi, , Zhong-Ming Niu et al.

- [Cross-section prediction for isotopes near neutron drip line in \$^{70, 80}\text{Zn}\$ projectile fragmentation reactions](#)

Hui-Ling Wei, , Yi-Dan Song et al.

- [Microscopic study of electromagnetic properties and band spectra of neutron deficient \$^{133,135,137}\text{Sm}\$](#)

Rakesh K. Pandit, R.K. Bhat, Rani Devi et al.

Production of exotic neutron-deficient isotopes near $N, Z = 50$ in multinucleon transfer reactions*

Xin-Xin Xu(许馨心)^{1,2} Gen Zhang(张根)^{1,2} Jing-Jing Li(李静静)^{1,2} Bing Li(李冰)^{1,2} Cheikh A. T. Sokhna^{1,2}
 Xin-Rui Zhang(张欣蕊)^{1,2} Xiu-Xiu Yang(杨秀秀)^{1,2} Shi-Hui Cheng(程诗慧)^{1,2} Yu-Hai Zhang(张钰海)^{1,2}
 Zhi-Shuai Ge(葛志帅)^{1,2} Cheng Li(李成)^{1,2} Zhong Liu(刘忠)³ Feng-Shou Zhang(张丰收)^{1,2,4;1)}

¹Key Laboratory of Beam Technology of Ministry of Education, College of Nuclear Science and Technology,
 Beijing Normal University, Beijing 100875, China

²Beijing Radiation Center, Beijing 100875, China

³Institute of Modern Physics, Chinese Academy of Sciences, Lanzhou 730000, China

⁴Center of Theoretical Nuclear Physics, National Laboratory of Heavy Ion Accelerator of Lanzhou, Lanzhou 730000, China

Abstract: The multinucleon transfer reaction in the collisions of $^{40}\text{Ca} + ^{124}\text{Sn}$ at $E_{\text{c.m.}} = 128.5$ MeV is investigated using the improved quantum molecular dynamics model. The measured angular distributions and isotopic distributions of the products are reproduced reasonably well by the calculations. The multinucleon transfer reactions of $^{40}\text{Ca} + ^{112}\text{Sn}$, $^{58}\text{Ni} + ^{112}\text{Sn}$, $^{106}\text{Cd} + ^{112}\text{Sn}$, and $^{48}\text{Ca} + ^{112}\text{Sn}$ are also studied. This demonstrates that the combinations of neutron-deficient projectile and target are advantageous for the production of exotic neutron-deficient nuclei near $N, Z = 50$. The charged particles' emission plays an important role at small impact parameters in the de-excitation processes of the system. The production cross sections of the exotic neutron-deficient nuclei in multinucleon transfer reactions are much larger than those measured in the fragmentation and fusion-evaporation reactions. Several new neutron-deficient nuclei can be produced in the $^{106}\text{Cd} + ^{112}\text{Sn}$ reaction. The corresponding production cross sections for the new neutron-deficient nuclei, $^{101, 112}\text{Sb}$, ^{103}Te , and $^{106, 107}\text{I}$, are 2.0 nb, 4.1 nb, 6.5 nb, 0.4 μb and 1.0 μb , respectively.

Keywords: production cross- sections, exotic neutron-deficient nuclei, production cross sections

PACS: 25.40.Hs, 25.70.-z **DOI:** 10.1088/1674-1137/43/6/064105

1 Introduction

The production of the neutron-deficient nuclei near $N, Z = 50$ has attracted extensive attention in recent years [1-6]. On the one hand, the structure and decay properties of these nuclei play special roles in nuclear physics. For the nuclei with $N \approx Z$ around the doubly magic nucleus ^{100}Sn , the valence neutrons and protons occupy the same orbits. Therefore, the neutron-proton pairing correlations are greatly enhanced. The level structure of the nuclei below ^{100}Sn is well described in the basic shell model space with a rigid core at $N = Z = 50$ and valence holes. The core-excited states have been observed in semimagic nuclei including ^{95}Rh , ^{96}Pd , ^{97}Ag , ^{98}Cd , etc. [7-9]. The decay properties of the neutron-deficient nuclei around ^{100}Sn have revealed interesting phenomena, such as the Gamow-Teller transition, proton decay, two-proton decay, α de-

cay, etc [10-13]. In addition, the clusters ($Z \geq 3$) emission from the excited state of nuclei has been observed in this region. On the other hand, the rp-process (a sequence of proton captures followed by β^+ decays) runs along the $N = Z$ line, which is believed to be responsible for the production of stable isotopes on the neutron-deficient side of the valley of β stability. The production of these nuclei is also extremely important to understand the rp-process in nuclear astrophysics [14-16].

The fragmentation reactions of ^{238}U at intermediate and relativistic energies produce the new neutron-rich nuclei with a wide range [17-20]. However, the new neutron-deficient nuclei near ^{100}Sn are obtained through the fragmentation of the neutron-deficient projectile, such as ^{106}Cd , ^{112}Sn , and ^{124}Xe . Many such experiments were performed at RIKEN [6], GSI [21], MSU [22], and GANIL [23]. For example, four new nuclei, ^{96}In , ^{94}Cd , ^{92}Ag , and

Received 4 March 2019, Published online 25 April 2019

* Supported by National Natural Science Foundation of China (11635003, 11025524, 11161130520), the National Basic Research Program of China (2010CB832903) and the European Commissions 7th Framework Programme (FP7-PEOPLE-2010-IRSES) (269131)

1) E-mail: fszhang@bnu.edu.cn

©2019 Chinese Physical Society and the Institute of High Energy Physics of the Chinese Academy of Sciences and the Institute of Modern Physics of the Chinese Academy of Sciences and IOP Publishing Ltd

^{90}Pd , were observed with cross sections about $10^{-12} - 10^{-11}\text{mb}$ by using a 345 MeV/A ^{124}Xe beam impinging on a Be target at RIKEN [6]. The ^{100}Sn was also identified in this experiment with the production cross-section at about 10^{-9} mb . Another method to produce the nuclei near ^{100}Sn is the fusion-evaporation reaction of stable neutron-deficient partners such as ^{63}Cu ($^{40}\text{Ca}, 3\text{n}$) ^{100}In [24], ^{58}Ni ($^{50}\text{Cr}, \alpha p3n$) ^{100}In [25], ^{58}Ni ($^{58}\text{Ni}, 12\text{C3n}$) ^{101}Sn [25], etc. The cluster and light charged particles emissions play an important role in the de-excitation processes of the neutron-deficient compound nucleus. In Ref. [26], ^{100}Sn was observed in the fusion-evaporation reaction of 255 MeV ^{50}Cr with ^{58}Ni at GANIL. The reported production cross-section of ^{100}Sn was 10^{-5} mb . Recently, the reaction ^{54}Fe ($^{58}\text{Ni}, 4\text{n}$) ^{108}Xe was performed at the ATLAS facility of Argonne National Laboratory using the Fragment Mass Analyzer (FMA). The self-conjugate $^{108}\text{Xe} \rightarrow ^{104}\text{Te} \rightarrow ^{100}\text{Sn}$ α -decay chain was observed for the first time [27].

The multinucleon transfer (MNT) reaction is used to generate the exotic nuclei far from the β stability line, including not only the neutron-rich nuclei, but also the neutron-deficient nuclei. For example, the new neutron-deficient nuclei, ^{216}U , ^{219}Np , ^{223}Am , ^{229}Am , and ^{233}Bk , were produced in the MNT reaction of $^{48}\text{Ca} + ^{248}\text{Cm}$ at GSI [28]. In Ref. [29], another MNT reaction of $^{136}\text{Xe} + ^{198}\text{Pt}$ at 7.98 MeV/A showed that the production cross-sections of the neutron-rich nuclei with $N=126$ are much larger than those measured in the fragmentation reaction of $^{208}\text{Pb} + ^9\text{Be}$ at 1 GeV/A [30]. Beside the experimental achievements, some models have been developed to describe MNT processes during the recent years. The ImQMD model is a semiclassical microscopic dynamics model based on effective nucleon-nucleon interaction, which is successfully applied to heavy-ion collisions at intermediate and low energies [31-33]. Other models for describing the MNT reactions include the Complex WKB (CWKB) theory [34, 35], the isospin-dependent quantum molecular dynamics model (IQMD) [36-40], the dinuclear system (DNS) model [41-48], etc. For a comprehensive review, please read Ref. [49].

In this study, we attempt to produce the neutron-deficient nuclei near $N, Z = 50$ with MNT reactions using the ImQMD model. The structure of this paper is as follows. In Sec. 2, we briefly introduce the ImQMD model. The results and discussion are presented in Sec. 3. Finally the conclusion is given in Sec. 4.

2 Theoretical framework

In the ImQMD model, as in the original QMD model [50], each nucleon is represented by a coherent state of a Gaussian wave packet

$$\phi_i(\mathbf{r}) = \frac{1}{(2\pi\sigma_r^2)^{3/4}} \exp\left[-\frac{(\mathbf{r}-\mathbf{r}_i)^2}{4\sigma_r^2} + \frac{i}{\hbar} \mathbf{r} \cdot \mathbf{p}_i\right], \quad (1)$$

where \mathbf{r}_i and \mathbf{p}_i are the centers of the i th wave packet in the coordinate and momentum space, respectively. σ_r represents the spatial spread of the wave packet in the coordinate space. The time evolution of \mathbf{r}_i and \mathbf{p}_i for each nucleon is governed by Hamiltonian equations of motion

$$\dot{\mathbf{r}}_i = \frac{\partial H}{\partial \mathbf{p}_i}, \quad \dot{\mathbf{p}}_i = -\frac{\partial H}{\partial \mathbf{r}_i}. \quad (2)$$

The Hamiltonian of the system includes the kinetic energy $T = \sum_i \frac{\mathbf{p}_i^2}{2m}$ and effective interaction potential energy

$$H = T + U_{\text{Coul}} + U_{\text{loc}}, \quad (3)$$

where U_{Coul} is the Coulomb energy, which is written as the sum of the direct and the exchange contribution

$$U_{\text{Coul}} = \frac{1}{2} \int \int \rho_p(\mathbf{r}) \frac{e^2}{|\mathbf{r} - \mathbf{r}'|} \rho_p(\mathbf{r}') d\mathbf{r} d\mathbf{r}' - e^2 \frac{3}{4} \left(\frac{3}{\pi}\right)^{1/3} \int \rho_p^{4/3} d\mathbf{r}. \quad (4)$$

Here, ρ_p is the density distribution of protons in the system. The nuclear interaction potential energy U_{loc} is obtained from the integration of the Skyrme energy density functional $U = \int V_{\text{loc}}(\mathbf{r}) d\mathbf{r}$ without the spin-orbit term, which reads

$$V_{\text{loc}} = \frac{\alpha}{2\rho_0} \frac{\rho^2}{\rho_0} + \frac{\beta}{\gamma+1} \frac{\rho^{\gamma+1}}{\rho_0^\gamma} + \frac{g_{\text{sur}}}{2\rho_0} (\nabla \rho)^2 + \frac{C_s}{2\rho_0} (\rho^2 - \kappa_s (\nabla \rho)^2) \delta^2 + g_\tau \frac{\rho^{\eta+1}}{\rho_0^\eta}. \quad (5)$$

Here, $\rho = \rho_n + \rho_p$ is the nucleon density. $\delta = (\rho_n - \rho_p)/(\rho_n + \rho_p)$ is the isospin asymmetry. The first three terms in the above expression are directly obtained from the Skyrme interaction. The fourth term denotes the symmetry potential energy including the bulk and surface symmetry potential energies. The last term is a small correction term. The parameters named IQ2 (see Table 1) adopted in this work have been tested for describing the fusion reactions [51], MNT reactions [31-33, 52], and fragmentation reactions [53]. The phase space occupation constraint method proposed by Papa et al. in the constrained molecular dynamics (CoMD) model [54] is adopted to describe the fermionic nature of the N -body system. This greatly improves the stability of an individual nucleus.

In this study, we set the z -axis as the beam direction and the x -axis as the impact parameter direction. The initial distance of the center of mass between the projectile and target is 30 fm. The wave-packet width is set as $\sigma_r = 1.2$ fm. The dynamic simulation is stopped at 1000 fm/c. Subsequently, the GEMINI code [55, 56] is used to deal with the subsequent de-excitation process. The evap-

Table 1. Model parameters (IQ2) adopted in this study.

α/MeV	β/MeV	γ	$g_{\text{sur}}/(\text{MeV} \cdot \text{fm}^2)$	g_T/MeV	η	C_S/MeV	κ_s/fm^2	ρ_0/fm^{-3}
-356	303	7/6	7.0	12.5	2/3	32.0	0.08	0.165

oration of the light particles is treated by the Hauser-Feshbach theory [57] including $n, p, d, t, {}^3\text{He}, {}^6\text{He}, {}^{6-8}\text{Li}$, and ${}^{7-10}\text{Be}$ channels. The level density in the GEMINI code is obtained by the Fermi gas expression

$$\rho(U, J) = (2J + 1) \left[\frac{\hbar^2}{2I} \right]^{3/2} \frac{\sqrt{a} \exp(2\sqrt{aU})}{12 U^2}, \quad (6)$$

where I is the moment-of-inertia of the residual nucleus or saddle-point configuration. The level density parameter was taken as $a = A/8 \text{ MeV}^{-1}$ as usual.

3 Results and discussion

To test the ImQMD model in terms of the description of MNT reactions, we calculate the collisions of ${}^{40}\text{Ca} + {}^{124}\text{Sn}$ at $E_{\text{c.m.}} = 128.5 \text{ MeV}$. The range of the impact parameters in the calculations is from 0 to b_{max} fm. $b_{\text{max}} = R_P + R_T$, where R_P and R_T denote the radii of the projectile and target, respectively. The incident energy is slightly higher than the Coulomb barrier (120.1 MeV). For central collisions, most events are fusion reactions. Fusion and elastic scattering events are not taken into account in our analysis. Figure 1 shows that the angular distributions of the final projectile-like-fragments (PLFs) with different transfer channels in ${}^{40}\text{Ca} + {}^{124}\text{Sn}$ at $E_{\text{c.m.}} = 128.5 \text{ MeV}$. The grazing angle in the laboratory frame is 75° . The calculated maximum of the cross-sec-

tions decreases more quickly with increasing neutron pickup channel than the experimental data [34]. However, the positions of the maximum are always consistent with the experimental data, which are locate at the grazing angle with a small dependence on the channel.

Figure 2 shows the production cross-sections of the final PLFs in the ${}^{40}\text{Ca} + {}^{124}\text{Sn}$ reaction at $E_{\text{c.m.}} = 128.5 \text{ MeV}$. The squares and folding lines denote the calculations of the ImQMD model and CWKB theory [34] following evaporation, respectively. The experimental data are taken from Ref. [34]. The measured isotopic cross-sections have been obtained by integrating the angular distributions by a quasi-Gaussian fit. Fig. 2 shows that the ImQMD calculations are in reasonable agreement with the corresponding experimental data. The discrepancies between the calculated and experimental data are generally within one order of magnitude. One sees that the CWKB calculations reproduce the experimental data very well at the neutron-rich side of the distributions for the proton stripping channels from $0p$ ($Z = 20$) to $-4p$ ($Z = 16$). However, the calculations grossly underestimate the cross-sections by several orders of magnitude at the neutron-deficient side. We do not show the calculations on the target-like-fragments (TLFs) because of the absence of experimental data. These results indicate that the ImQMD model is applicable for the study of MNT reactions in intermediate-mass systems.

In order to produce the neutron-deficient nuclei near

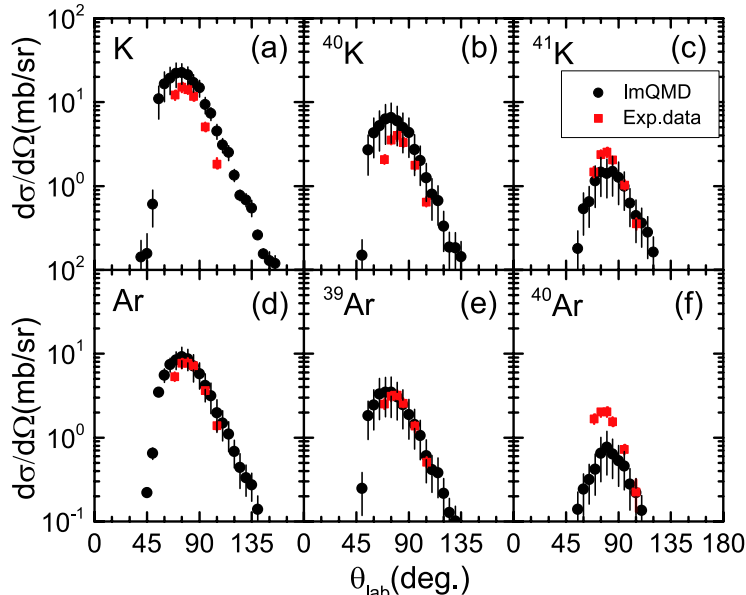


Fig. 1. (color online) Angular distributions of the final PLFs with different transfer channels in ${}^{40}\text{Ca} + {}^{124}\text{Sn}$ at $E_{\text{c.m.}} = 128.5 \text{ MeV}$. The experimental data are taken from Ref. [34].

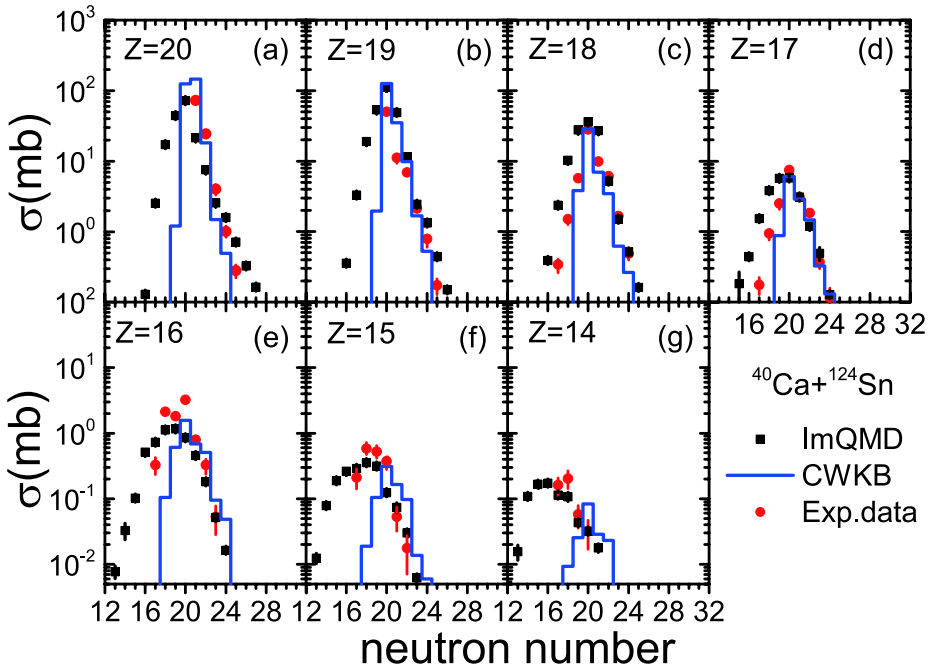


Fig. 2. (color online) Production cross sections of the final PLFs in $^{40}\text{Ca} + ^{124}\text{Sn}$ at $E_{\text{c.m.}} = 128.5$ MeV. The black squares and folding lines denote the calculations of the ImQMD model and CWKB theory [34] following evaporation, respectively. The experimental data are taken from Ref. [34].

$N, Z = 50$, choosing a favorable projectile-target combination is very important. Considering that the production cross sections at the maximum of the isotopic distributions decrease rapidly with increasing proton transfer channel, we choose the neutron-deficient nuclei, ^{106}Cd and ^{112}Sn , as targets. Figure 3 shows the calculated production cross-sections of final TLFs with charge numbers from $Z = 50$ to 54 in reactions of $^{48}\text{Ca} + ^{112}\text{Sn}$, $^{40}\text{Ca} + ^{112}\text{Sn}$, $^{58}\text{Ni} + ^{112}\text{Sn}$, and $^{106}\text{Cd} + ^{112}\text{Sn}$. The production cross-sections of the exotic neutron-deficient nuclei are the smallest in the $^{48}\text{Ca} + ^{112}\text{Sn}$ system, hence this system is not suitable to produce such nuclei. For $^{40}\text{Ca} + ^{112}\text{Sn}$, $^{58}\text{Ni} + ^{112}\text{Sn}$, and $^{106}\text{Cd} + ^{112}\text{Sn}$ reactions, one can see that the discrepancies of the cross-sections in the neutron-rich side are very significant. This is because the cross-section in the neutron-rich side is very sensitive to the N/Z value of the projectile. The N/Z values for ^{40}Ca , ^{58}Ni , and ^{106}Cd are 1.00, 1.07, and 1.21, respectively. Therefore, the production cross-sections of neutron-rich isotopes in $^{106}\text{Cd} + ^{112}\text{Sn}$ are larger than those in the other two reactions. The isotopic distributions are similar for the three systems in the neutron-deficient side. This is because the primary distributions of three systems are almost the same in the neutron-deficient side.

In MNT reactions, the energy dissipation process is a complex issue. The excitation energy of the reaction products plays an important role in their de-excitation processes. In the ImQMD model, the excitation energy of an excited fragment is calculated as $E^* = E_{\text{tot}} - E_b$. Here,

E_{tot} and E_b denote the total and binding energies in the ground state, respectively. The total energy of a fragment is the sum of all kinetic and potential energy of a nucleon in the body frame. Figure 4(a) shows the average excitation energy of the products in binary events as a function of the impact parameters in $^{106}\text{Cd} + ^{112}\text{Sn}$ at $E_{\text{c.m.}} = 500$ MeV. In the region of $b \geq 6$ fm, the total excitation energy of the system increases rapidly with decreasing impact parameters, until it reaches a saturation value (about 145 MeV) at $b < 5$ fm. The decay properties of the nuclei near the ^{100}Sn are markedly different with neutron-rich nuclei. In the experiment, the emissions of proton and α particles were observed in the decay processes of some specific nuclei even in their ground state. For the de-excitation processes of these nuclei in excited states, the decay channels would be more complex. Figure 4(b) shows the yields of n , p , d , t , ^3He , and α particles as a function of impact parameters in the $^{106}\text{Cd} + ^{112}\text{Sn}$ system at $E_{\text{c.m.}} = 500$ MeV. The charged particles' emission plays an important role at small impact parameters in the de-excitation processes of the system. The number of emitted protons are much greater than that of other emitted charged particles. In the GEMINI simulation, we find that the protons emission is the main decay channel for exotic neutron-deficient nuclei. In addition, the yields of the α and d particles are considerable at small impact parameters. This results in a decrease of the yield of neutrons with a decrease in the impact parameter at $b < 6$ fm. Figure 4(c) illustrates the cross-sections for the forma-

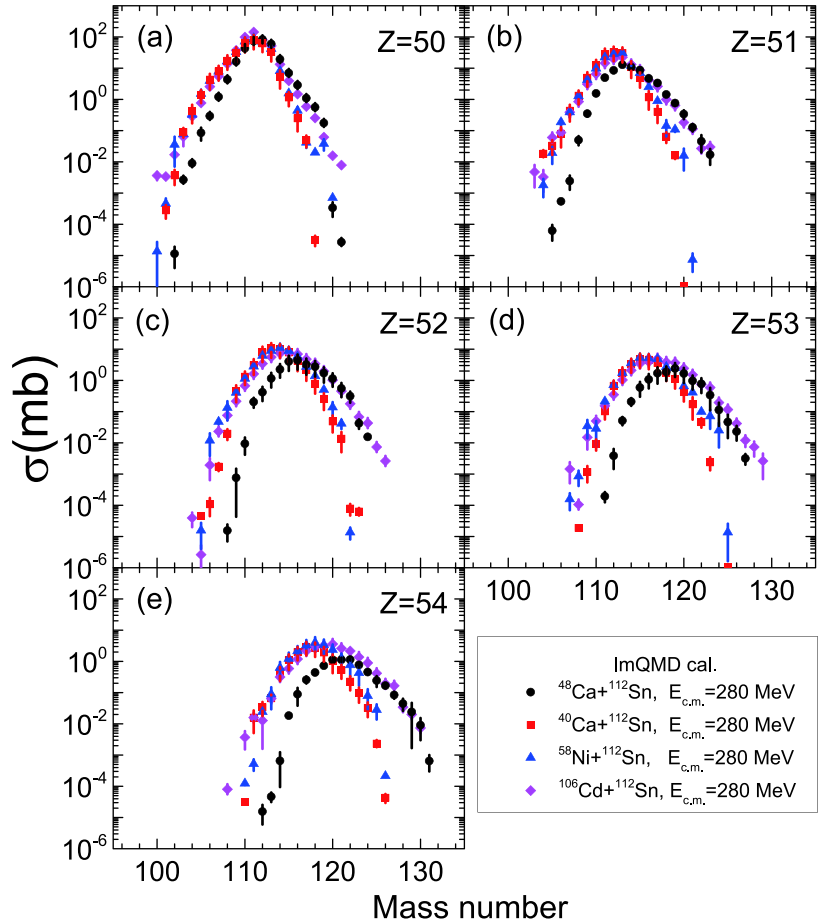


Fig. 3. (color online) Calculated production cross sections of final TLFs with charge number from $Z = 50$ to 54 in different reactions at $E_{\text{c.m.}} = 280 \text{ MeV}$.

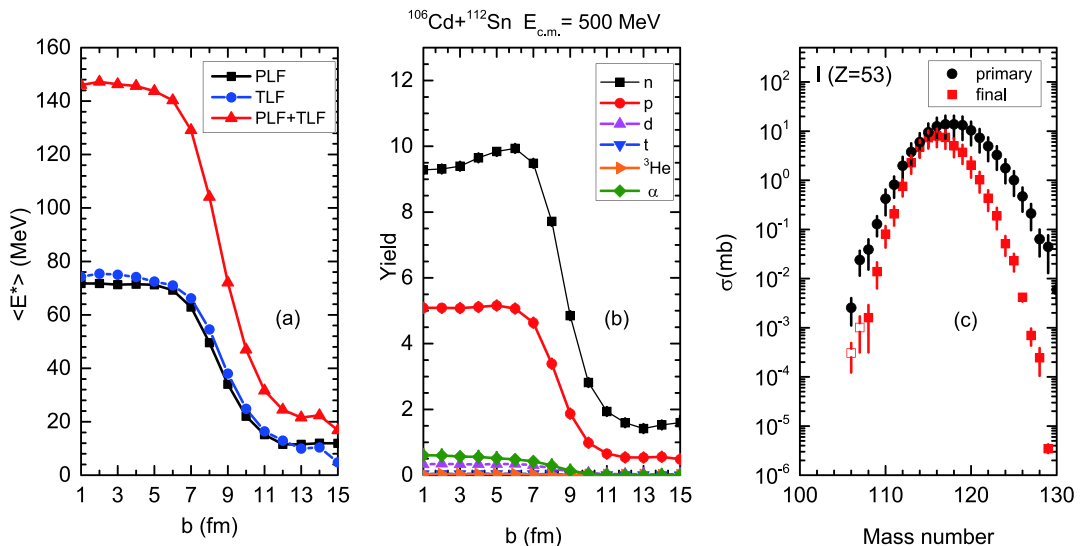


Fig. 4. (color online) (a) Average excitation energy of the products in binary events as a function of impact parameters in $^{106}\text{Cd} + ^{112}\text{Sn}$ at $E_{\text{c.m.}} = 500 \text{ MeV}$. (b) Yields of n , p , d , t , ^3He , and α particles as a function of impact parameters in the $^{106}\text{Cd} + ^{112}\text{Sn}$ system at $E_{\text{c.m.}} = 500 \text{ MeV}$. (c) Cross-sections for formation of iodine isotopes ($Z = 53$) in collision of $^{106}\text{Cd} + ^{112}\text{Sn}$ at $E_{\text{c.m.}} = 500 \text{ MeV}$. Solid circles and squares denote the distribution of primary and final fragments, respectively. Open squares denote the unknown neutron-deficient isotopes.

tion of iodine isotopes ($Z = 53$) in the collisions of $^{106}\text{Cd} + ^{112}\text{Sn}$ at $E_{\text{c.m.}} = 500$ MeV. The open squares depict the unknown proton-rich nuclei. The final yields shift to the neutron-deficient side after the de-excitation process. More neutrons are evaporated on the neutron-rich side than on the neutron-deficient side after the de-excitation process. This is because the neutron emission is the dominant decay channel for neutron-rich nuclei.

Figure 5 shows the calculated isotopic distributions of final TLFs with charge number from $Z = 50$ to 54 by the ImQMD model in the reactions of $^{106}\text{Cd} + ^{112}\text{Sn}$ at $E_{\text{c.m.}} = 300, 500$, and 780 MeV. The isotopic production cross-sections in the neutron-rich side become lower with increasing incident energies. The neutron evaporation is the main decay channel for the primary neutron-rich products. In the case of larger incident energy, this causes a larger shift of final distributions to the neutron-deficient side. While in the neutron-deficient side, isotopic distributions are almost the same for these three incident energies. Generally, larger incident energy improves the transfer probability of nucleons, which leads to a larger production cross-section for the primary neutron-deficient nuclei. However, the survival probability of these nuclei is lower due to higher excitation energies. If the incident energy continues to increase, the production cross-sections of the exotic neutron-deficient nuclei should be

reduced, because the reactions are dominated by fragmentation mechanisms.

Table 2 shows the comparison of calculated production cross-sections for exotic neutron-deficient nuclei from the MNT reactions with measured values from the fragmentation and fusion-evaporation reactions. The measured cross-sections from the fragmentation method are obtained in the reaction of 345 MeV/A $^{124}\text{Xe} + \text{Be}$ [2, 6]. For the fusion-evaporation method, the cross sections of ^{100}In and ^{101}Sn are measured in the $^{58}\text{Ni} + ^{58}\text{Ni}$ system [25] at $E_{\text{lab}} = 348$ MeV; ^{100}Sn is measured in $^{50}\text{Cr} + ^{58}\text{Ni}$ [26] at $E_{\text{lab}} = 255$ MeV; ^{108}I , ^{109}Xe , and ^{110}Xe are measured in $^{58}\text{Ni} + ^{54}\text{Fe}$ [58] at $E_{\text{lab}} = 255, 200$, and 215 MeV, respectively. The cross-sections of these isotopes from the MNT method are calculated with $^{106}\text{Cd} + ^{112}\text{Sn}$ at $E_{\text{c.m.}} = 500$ MeV using the ImQMD model. For the fusion-evaporation reactions, the production cross sections of the residual nucleus are one or two orders of magnitude lower than those from the multinucleon transfer reactions. For the projectile fragmentation, the production cross-sections of these nuclei are much lower. For example, the cross-sections of ^{100}Sn by projectile fragmentation is only on the order of 10^{-10} millibarn. Therefore, the MNT reactions have advantages in comparison to fusion-evaporation and projectile fragmentation reactions. **Figure 6** shows the neutron-deficient nuclei region around

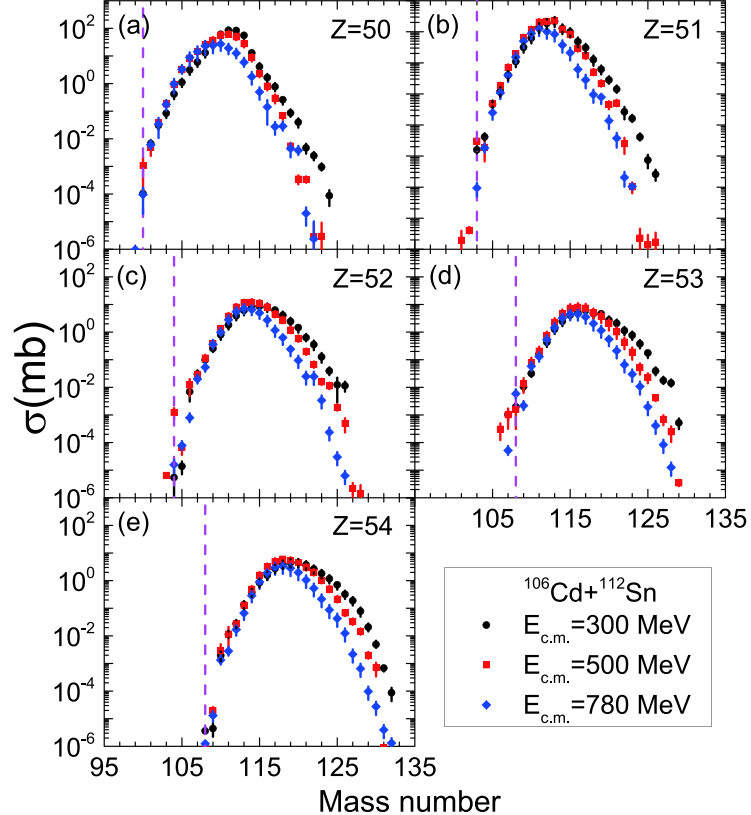


Fig. 5. (color online) Calculated isotopic distributions of final fragments by the ImQMD model in reactions of $^{106}\text{Cd} + ^{112}\text{Sn}$ at $E_{\text{c.m.}} = 300, 500$, and 780 MeV. Dashed lines indicate the boundaries of known isotopes.

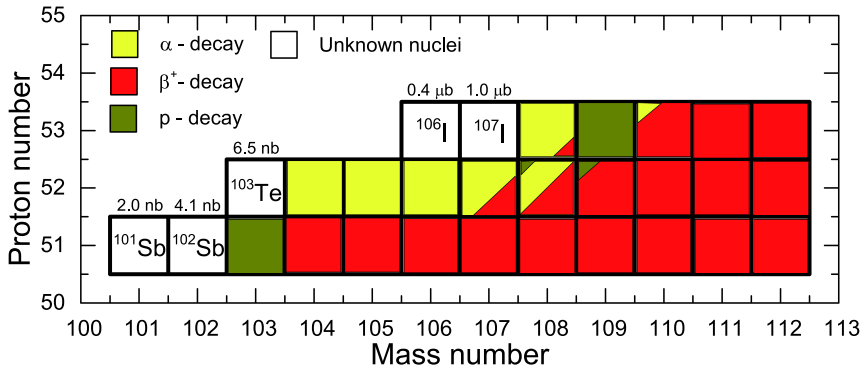


Fig. 6. (color online) Neutron-deficient nuclei region around ^{100}Sn on the nuclear map. Filled and open squares denote known and predicted nuclei, respectively. Yellow, red, and olive colors indicate the α decay, β^+ decay, and proton decay, respectively. The production cross-sections in the reaction of $^{106}\text{Cd} + ^{112}\text{Sn}$ at $E_{\text{c.m.}} = 500$ MeV are depicted in the graph.

Table 2. Comparison of calculated production cross-sections for exotic neutron-deficient nuclei from MNT reactions with measured values from fragmentation and fusion-evaporation reactions.

isotope	$\sigma_{\text{frag}}^{\text{expt}}/\text{mb}$	$\sigma_{\text{fus}}^{\text{expt}}/\text{mb}$	$\sigma_{\text{MNT}}^{\text{theo}}/\text{mb}$
^{97}In	1.3×10^{-10} [6]	–	7.2×10^{-6}
^{98}In	1.4×10^{-8} [6]	–	3.5×10^{-3}
^{99}In	2.2×10^{-7} [2]	–	2.0×10^{-2}
^{100}In	8.6×10^{-6} [2]	1.7×10^{-3} [25]	3.8×10^{-2}
^{100}Sn	7.4×10^{-10} [2]	4.0×10^{-5} [26]	1.1×10^{-3}
^{101}Sn	4.0×10^{-8} [2]	1.3×10^{-5} [25]	5.0×10^{-3}
^{102}Sn	2.2×10^{-6} [2]	–	3.9×10^{-2}
^{103}Sn	7.7×10^{-5} [2]	–	1.8×10^{-1}
^{104}Sb	3.5×10^{-7} [2]	–	1.9×10^{-3}
^{105}Te	1.2×10^{-9} [2]	–	6.6×10^{-5}
^{106}Te	1.3×10^{-7} [2]	–	1.2×10^{-2}
^{108}I	–	8.6×10^{-4} [58]	1.6×10^{-3}
^{109}Xe	–	1.0×10^{-5} [58]	2.0×10^{-5}
^{110}Xe	–	1.0×10^{-3} [58]	3.0×10^{-3}

^{100}Sn on the nuclear map. The filled and open squares denote the known and the predicted nuclei, respectively. Yellow, red, and olive colors indicate α decay, β^+ decay, and proton decay, respectively. The production cross-sections with the ImQMD model in the reaction of $^{106}\text{Cd} + ^{112}\text{Sn}$ at $E_{\text{c.m.}} = 500$ MeV are signed in the graph. Several new neutron-deficient nuclei are produced in the $^{106}\text{Cd} + ^{112}\text{Sn}$ reaction. The corresponding production cross-sections for the new neutron-deficient nuclei, $^{101}, ^{102}\text{Sb}$, ^{103}Te ,

and $^{106}, ^{107}\text{I}$, are 2.0 nb, 4.1 nb, 6.5 nb, 0.4 μb and 1.0 μb , respectively.

4 Conclusions

The production cross-sections and angular distributions of PLFs in the reaction of $^{40}\text{Ca} + ^{124}\text{Sn}$ at $E_{\text{c.m.}} = 128.5$ MeV are calculated by the ImQMD model. The results show that the ImQMD model is suitable to describe the MNT reactions of the intermediate-mass systems. To produce the exotic neutron-deficient nuclei around $N, Z = 50$, the multinucleon transfer reactions of $^{48}\text{Ca} + ^{112}\text{Sn}$, $^{40}\text{Ca} + ^{112}\text{Sn}$, $^{58}\text{Ni} + ^{112}\text{Sn}$, and $^{106}\text{Cd} + ^{112}\text{Sn}$ are studied. We find that combinations of neutron-deficient projectile and target are advantageous for the production of the exotic neutron-deficient nuclei. The distribution of the final production cross-section of exotic neutron-deficient nuclei is similar in the reactions of $^{106}\text{Cd} + ^{112}\text{Sn}$ at $E_{\text{c.m.}} = 300, 500$, and 780 MeV. The de-excitation processes of the $^{106}\text{Cd} + ^{112}\text{Sn}$ system at $E_{\text{c.m.}} = 500$ MeV are analysed. The charged particles' emission plays an important role for the highly excited system. Proton emission is the main decay channel in the de-excitation processes of exotic neutron-deficient nuclei. Compared to the fragmentation and fusion-evaporation reactions, the MNT reaction is highly advantageous for the production of the neutron-deficient nuclei around $N, Z = 50$. The cross-sections of unknown neutron-deficient isotopes $^{101}, ^{102}\text{Sb}$, ^{103}Te , and $^{106}, ^{107}\text{I}$ are 2.0 nb, 4.1 nb, 6.5 nb, 0.4 μb and 1.0 μb in the $^{106}\text{Cd} + ^{112}\text{Sn}$ reaction, respectively.

References

- V.-V. Elomaa, T. Eronen, U. Hager et al, *Eur. Phys. J. A*, **40**: 1 (2009)
- H. Suzuki, T. Kubo, N. Fukuda et al, *Nucl. Instr. Meth. Phys. Res. B*, **317**: 756 (2013)
- Sh. A. Kalandarov, G. G. Adamian, N. V. Antonenko et al, *Phys. Rev. C*, **90**: 024609 (2014)
- P. Doornenbal, S. Takeuchi, N. Aoi et al, *Phys. Rev. C*, **90**: 061302(R) (2014)

- 5 A. Johnson, Eur. Phys. J. A, **13**: 9 (2002)
- 6 I. Čeliković, M. Lewitowicz, R. Gernhäuser et al, Phys. Rev. Lett., **116**: 162501 (2016)
- 7 H. A. Roth, S. E. Arnell, D. Foltescu et al, Phys. Rev. C, **50**: 1330 (1994)
- 8 M. Palacz, J. Nyberg, H. Grawe et al, Phys. Rev. C, **86**: 014318 (2012)
- 9 M. Lipoglavšek, M. Vencelj, C. Baktash et al, Phys. Rev. C, **72**: 061304(R) (2005)
- 10 C. B. Hinke, M. Böhmer, P. Boutachkov et al, Nature (London), **486**: 341 (2012)
- 11 R. D. Page, P. J. Woods, R. A. Cunningham et al, Phys. Rev. C, **49**: 3312 (1994)
- 12 R. Kirchner, O. Klepper, G. Nyman et al, Phys. Lett. B, **70**: 150 (1977)
- 13 C. Xu and Z. Z. Ren, Phys. Rev. C, **74**: 037302 (2006)
- 14 H. Schatz, A. Aprahamian, J. Görres et al, Phys. Rep., **294**: 167 (1998)
- 15 H. Schatz, A. Aprahamian, V. Barnard et al, Phys. Rev. Lett., **86**: 3471 (2001)
- 16 C. Mazzocchi, R. Grzywacz, S. N. Liddick et al, Phys. Rev. Lett., **98**: 212501 (2007)
- 17 J. Kurcewicz, F. Farinon, H. Geissel et al, Phys. Lett. B, **717**: 371 (2012)
- 18 J. Wu, S. Nishimura, G. Lorusso et al, Phys. Rev. Lett., **118**: 072701 (2017)
- 19 N. Fukuda, T. Kubo, D. Kameda et al, J. Phys. Soc. Jpn., **87**: 014202 (2018)
- 20 Y. Shimizu, T. Kubo, N. Fukuda et al, J. Phys. Soc. Jpn., **87**: 014203 (2018)
- 21 R. Schneider, J. Friese, J. Reinhold et al, Z. Phys. A, **348**: 241 (1994)
- 22 M. Hencheck, R. N. Boyd, M. Hellström et al, Phys. Rev. C, **50**: 2219 (1994)
- 23 K. Rykaczewski, R. Anne, G. Auger et al, Phys. Rev. C, **52**: R2310 (1995)
- 24 W. Kurcewicz, E. F. Zganjar, R. Kirchner et al, Z. Phys. A, **308**: 21 (1982)
- 25 M. La Commara, J. Gómez del Campo, A. DÓnofrio et al, Nucl. Phys. A, **669**: 43 (2000)
- 26 M. Chartier, G. Auger, W. Mittig et al, Phys. Rev. Lett., **77**: 2400 (1996)
- 27 K. Auranen, D. Seweryniak, M. Albers et al, Phys. Rev. Lett., **121**: 182501 (2018)
- 28 H. M. Devaraja, S. Heinz, O. Beliuskina et al, Phys. Lett. B, **748**: 199 (2015)
- 29 Y. X. Watanabe, Y. H. Kim, S. C. Jeong et al, Phys. Rev. Lett., **115**: 172503 (2015)
- 30 T. Kurtukian-Nieto, J. Benlliure, K.-H. Schmidt et al, Phys. Rev. C, **89**: 024616 (2014)
- 31 C. Li, P. W. Wen, J. J. Li et al, Phys. Lett. B, **776**: 278 (2018)
- 32 C. Li, X. X. Xu, J. J. Li et al, Phys. Rev. C, **99**: 024602 (2019)
- 33 C. Li, F. Zhang, J. J. Li et al, Phys. Rev. C, **93**: 014618 (2016)
- 34 L. Corradi, J. H. He, D. Ackermann et al, Phys. Rev. C, **54**: 201 (1996)
- 35 L. Corradi, A. M. Stefanini, D. Ackermann et al, Phys. Rev. C, **49**: 2875(R) (1994)
- 36 D. H. Zhang, W. J. Xie, J. Su et al, Chin. Phys. C, **39**: 044103 (2015)
- 37 L. W. Chen, F. S. Zhang, and G. M. Jin, Phys. Rev. C, **58**: 2283 (1998)
- 38 J. Su, C. Y. Huang, W. J. Xie et al, Eur. Phys. J. A, **52**: 207 (2016)
- 39 Z. Q. Feng, F. S. Zhang, G. M. Jin et al, Nucl. Phys. A, **750**: 232 (2018)
- 40 W. J. Xie and F. S. Zhang, Chin. Phys. C, **42**: 104103 (2015)
- 41 G. G. Adamian, N. V. Antonenko, V. V. Sargsyan et al, Phys. Rev. C, **81**: 057602 (2010)
- 42 F. Niu, P. H. Chen, Y. F. Guo et al, Phys. Rev. C, **96**: 064622 (2017)
- 43 L. Zhu, J. Su, W. J. Xie et al, Phys. Lett. B, **767**: 437 (2017)
- 44 L. Zhu, Chin. Phys. C, **41**: 124102 (2017)
- 45 X. J. Bao, S. Q. Guo, J. Q. Li et al, Phys. Lett. B, **785**: 221 (2018)
- 46 C. Li, P. W. Wen, J. J. Li et al, Nucl. Sci. Tech., **28**: 110 (2017)
- 47 L. Zhu, Z. Q. Feng, and F. S. Zhang, J. Phys. G Nucl. Part. Phys., **42**: 085102 (2015)
- 48 L. Zhu, J. Su, and F. S. Zhang, Nucl. Phys. A, **964**: 93 (2017)
- 49 F. S. Zhang, C. Li, L. Zhu et al, Front. Phys., **13**: 132113 (2018)
- 50 J. Aichelin, Phys. Rep., **202**: 233 (1991)
- 51 N. Wang, K. Zhao, and Z. X. Li, Phys. Rev. C, **90**: 054610 (2014)
- 52 K. Zhao, Z. X. Li, N. Wang et al, Phys. Rev. C, **92**: 024613 (2015)
- 53 C. Li, J. L. Tian, L. Ou et al, Phys. Rev. C, **87**: 064615 (2013)
- 54 M. Papa, T. Maruyama, and A. Bonasera, Phys. Rev. C, **64**: 024612 (2001)
- 55 R. J. Charity, M. A. McMahan, G. J. Wozniak et al, Nucl. Phys. A, **483**: 371 (1988)
- 56 R. J. Charity, Phys. Rev. C, **82**: 014610 (2010)
- 57 W. Hauser and H. Feshbach, Phys. Rev., **87**: 366 (1952)
- 58 A. Korgul, K. P. Rykaczewski, C. J. Gross et al, Phys. Rev. C, **77**: 034301 (2008)